A Novel Four-State Switchable Dual-Band Bandpass Filter with High OFF-State Suppression Based on Multi-Mode Resonators

Bingjie Yang[1], Zhongbao Wang[1, 2, *], Hongmei Liu[1], Mingming Gao[1, 2], and Shaojun Fang[1]

[1]*School of Information Science and Technology*
Dalian Maritime University, Dalian, Liaoning 116026, China
[2]*Liaoning Key Laboratory of Radio Frequency and Big Data for Intelligent Applications*
Liaoning Technical University, Huludao, Liaoning 125105, China

ABSTRACT: A novel switchable dual-band bandpass filter (BPF) is proposed, where each passband can be independently controlled. The filter is composed of a tri-mode resonator, a dual-mode resonator, and feed lines coupling with the resonators. By controlling the PIN diodes loaded on the open end of the resonators, four operating states (i.e., dual bands, lower passband, upper passband, and all-stop band) are realized. A switchable dual-band BPF prototype is designed, fabricated, and measured with the center frequencies of 1.575 and 2.45 GHz having the bandwidths of 300 and 220 MHz, respectively. The prototype occupies an area of $0.128\lambda_g^2$, where λ_g is the guided wavelength at the center frequency of the lower band (1.575 GHz). The measurement results indicate that the proposed switchable dual-band BPF has low insertion loss and high OFF-state suppression.

1. INTRODUCTION

Filters and radio frequency (RF) switches are two important components of microwave communication systems [1–4]. In today's increasingly crowded spectrum, people hope that RF devices can achieve more functions in limited space. Therefore, multi-band and switching functions are combined to form switchable filters, which can provide multi-band response and multi-state operation. In recent years, many circuit topologies for switchable bandpass filters (BPFs) have been proposed to achieve various functions [5–12]. For example, a novel microstrip switchable BPF has been proposed in [5], which achieves three filtering states by controlling the on/off of the switch to increase or decrease the number of branches: broadband BPF, dual-band BPF, and triple-band BPF. In [6], a switchable filter consists of a switchable band stop/total stop filter and a switchable dual-mode resonator (DMR), achieving multiple operating modes.

As an important branch of switchable filters, switchable dual-band BPFs have attracted widespread attention. Based on this, many design schemes for dual-band switchable BPF have been proposed [13–15]. In [13], a dual-band switchable BPF based on controllable grounding topology was proposed, which achieved fast tuning speed but had unsatisfactory insertion loss (IL) and matching performance, and could not simultaneously close all passbands. In [15], only three diodes were used to achieve four independent control operating states, and the circuit size was reduced by sharing resonators. However, the OFF-state suppression (OSS) when turning off a single passband or all passbands was less than 30 dB. In addition, some

design schemes for switchable multiband filters have also been proposed [16–18]. In [16], four modes can be switched by parallelizing two dual-band BPFs, and the number of dual-band BPFs can be expanded to N. Similarly, [17] and [18] can also switch between two types of dual-band BPFs. However, it cannot achieve independent control of each passband and enable or disable all passbands simultaneously. It can be seen that previous designs could not achieve simultaneous disabling of all frequency bands or have poor OSS performance when all frequency bands were disabled [16]. In addition, most designed multiband switchable filters suffer from high IL and poor return loss (RL) performance. Equally important, each passband needs to be guaranteed to be independently controllable. Based on the above research, for the design of multi-band switchable filters, it is necessary to maintain low IL and improve RL performance while ensuring that each frequency band can be independently enabled and disabled, as well as enhance the OSS performance when all frequency bands are simultaneously disabled.

This paper proposes an independently switchable dual-band BPF. The filter is composed of a DMR, a tri-mode resonator (TMR), and feed lines. The mode switching is achieved by controlling the PIN diodes loaded at the open end of the resonators. Finally, a dual-band BPF mode, two single-band BPF modes, and an all-stop filter (ASF) mode are achieved. The detailed design process is provided below.

2. THEORETICAL ANALYSIS AND DESIGN STRATEGY

A dual-band switchable BPF with high OSS suppression performance based on multi-mode resonators is proposed, and its
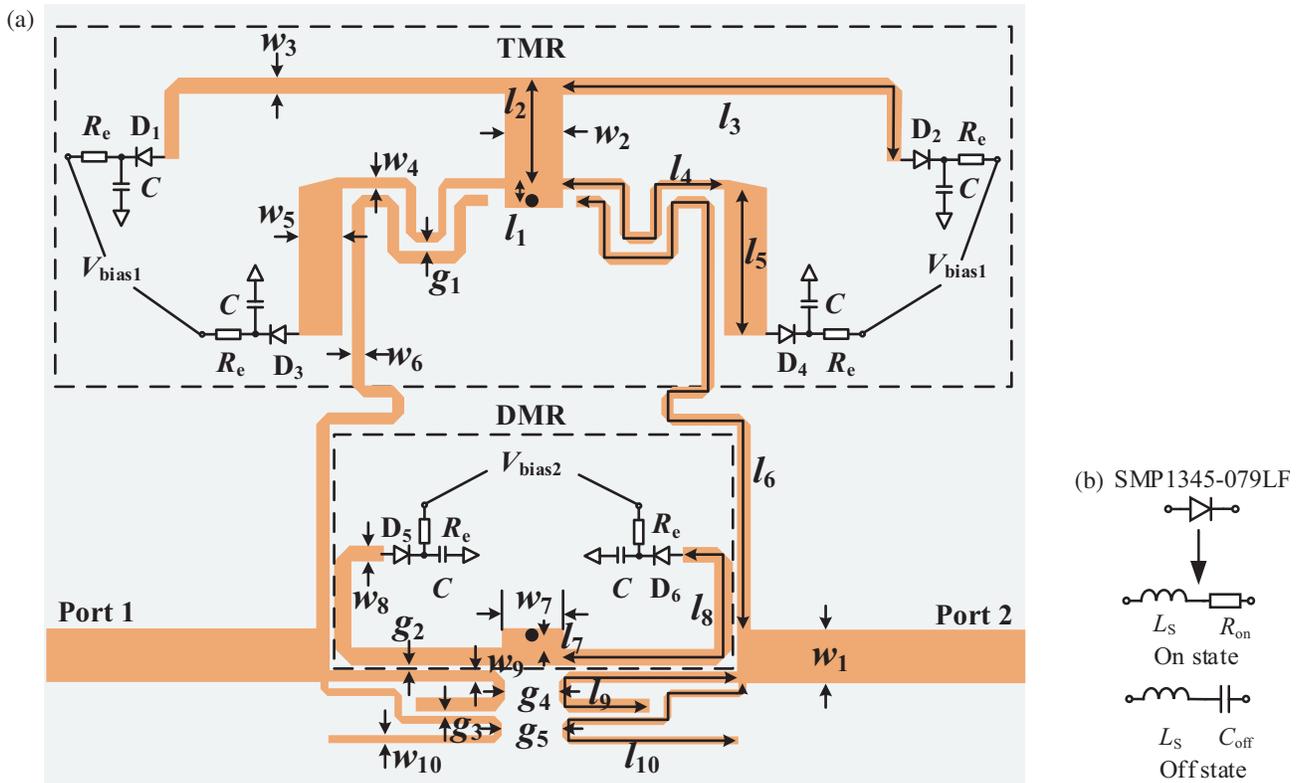

FIGURE 1. (a) Layout of the proposed switchable dual-band BPF. (b) Equivalent circuit model of PIN diode.

basic structure is shown in Fig. 1(a). Independent switching of four states is achieved by controlling the PIN diodes loaded at the open end of the resonators. The resonators consist of a TMR and a DMR, which are folded to make better use of space. The TMR forms the lower passband, and the DMR forms the upper passband. To save space, the feed lines have also been appropriately folded and coupled to supply energy to the resonators. Two types of resonators are arranged vertically and spaced apart to minimize interference between two passbands.

In the switching circuit, diodes D1–D6 use the SMP1345-079LF [19], and its equivalent circuit is shown in Fig. 1(b). When forward biased, the PIN diode is equivalent to a parasitic inductance and a small resistor connected in series, with the resonator grounded, resulting in a bandstop response in the corresponding branch. When reverse-biased, the PIN diode is equivalent to a parasitic inductance and a capacitor connected in series, which can be approximated as an open circuit. The parasitic series inductor is $L_s = 0.7 \, \text{nH}$; the forward-biased resistor is $R_{on} = 2 \, \Omega$; and the reverse-biased capacitor is $C_{off} = 0.15 \, \text{pF}$. The series resonant frequency of L_s and C_{off} is 15.53 GHz, which is out of the frequency range of concern for the filter. A 100 pF capacitor C is used to bypass the RF signal, making it ineffective against the DC voltage on the resistor. The current limiting resistor $R_e = 2 \, \text{k}\Omega$ acts together with the bias voltage V_{bias} on the diode, controlling its on/off behavior.

2.1. Characteristics of the TMR

When the PIN diodes loaded at the open end of the TMR resonator are reverse-biased, the TMR is in operation. The TMR is symmetrically distributed, as shown in Fig. 2(a). The characteristic admittance of each branch is represented by Y_i, and its electrical length and physical length are represented by θ_i and l_i, respectively. It should be noted that when the diodes are reverse biased, the influence of diodes on the TMR resonator needs to be considered (i.e., the loaded admittance Y_{load}). When the TMR resonator is excited by odd mode, the symmetry plane can be regarded as an ideal electric wall, and its equivalent circuit is shown in Fig. 2(b). The equivalent admittance Y_{ino1} of the odd-mode equivalent circuit in Fig. 2(b) can be calculated as follows

$$Y_{ino1} = jY_5 \frac{Y_5 \tan \theta_4 \tan \theta_5 - Y_4}{Y_5 \tan \theta_4 + Y_4 \tan \theta_5} + Y_{load} \quad (1)$$

$$Y_{load} = \frac{j\omega C_{off}}{1 - \omega^2 L_s C_{off}} \quad (2)$$

When the TMR resonator is excited by even mode, the symmetry plane can be regarded as an ideal magnetic wall, equivalent to an open circuit. The equivalent admittance Y_{ine1} of the even-mode equivalent circuit in Fig. 2(c) can be calculated as follows
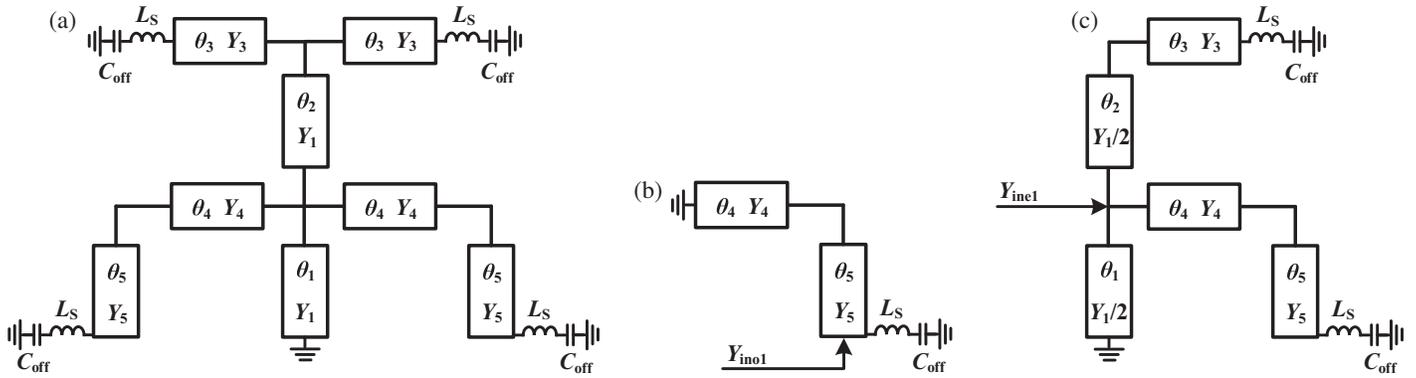
FIGURE 2. (a) Schematic of the TMR. (b) Odd-mode equivalent circuit. (c) Even-mode equivalent circuit.

$$Y_{ine1} = Y_{L1} + Y_{L2} + Y_{L3} \tag{3}$$

$$Y_{L1} = Y_4 \frac{\begin{array}{l} Y_5 \left(Y_{load} + jY_5 \tan\theta_5\right) \\ +jY_4 \tan\theta_4 \left(Y_5 + jY_{load} \tan\theta_5\right) \end{array}}{\begin{array}{l} Y_4 \left(Y_5 + jY_{load} \tan\theta_5\right) \\ +jY_5 \tan\theta_4 \left(Y_{load} + jY_5 \tan\theta_5\right) \end{array}} \tag{4}$$

$$Y_{L2} = \frac{-jY_1}{2 \tan\theta_1} \tag{5}$$

$$Y_{L3} = \frac{Y_1}{2} \frac{\begin{array}{l} 2Y_3 \left(Y_{load} + jY_3 \tan\theta_3\right) \\ +jY_1 \tan\theta_2 \left(Y_3 + jY_{load} \tan\theta_3\right) \end{array}}{\begin{array}{l} Y_1 \left(Y_3 + jY_{load} \tan\theta_3\right) \\ +2jY_3 \tan\theta_2 \left(Y_{load} + jY_3 \tan\theta_3\right) \end{array}} \tag{6}$$

When TMR resonates, $\text{Im}(Y_{ino1}) = 0$, $\text{Im}(Y_{ine1\_1}) = 0$, and $\text{Im}(Y_{ine1\_2}) = 0$. Let f_{0o1} be the self-resonant frequency under odd mode excitation, and f_{0e1} and f_{0e2} be the self-resonant frequencies under even mode excitation. f_{0o1} is determined by θ_4 and θ_5, and then f_{0e1} and f_{0e2} can be tuned by the electrical lengths θ_1, θ_2, and θ_3.

Figure 3 exhibits the effect of TMR's branch length on the self-resonant frequency. Since f_{0o1} is determined by l_4 and l_5, changing the lengths of l_1 and l_3 will hardly affect the self-resonant frequency f_{0o1}. It can be obtained that the resonant mode in the middle is f_{0o1}. The three self-resonant frequencies have the relationship of $f_{0e1} < f_{0o1} < f_{0e2}$. In addition, it can be observed that l_1 only affects f_{0e1}; the lengths of l_2 and l_3 affect two even resonant modes; and the length of l_4 affects three resonant modes. In summary, the following conclusion can be drawn: all branches of TMR will affect the first even resonant mode f_{0e1}. The second even resonant mode f_{0e2} is controlled by all branches except l_1. The odd mode resonant mode f_{0o1} is determined by l_4 and l_5. Adjust the length and width of each branch based on the above analysis to complete the design.

When the PIN diodes are forward-biased, the loaded admittance changes from Y_{load} in formula (2) to Y_{load_on} in formula (7).

$$Y_{load\_on} = \frac{R_{on} - j\omega L_s}{R_{on}^2 + \omega^2 L_s^2} \tag{7}$$

Due to changes in load admittance, the resonant state has changed (i.e., the resonant frequency of the TMR with forward-biased PIN diodes is greater than 3.2 GHz), resulting in a band-stop response before 3.2 GHz in the corresponding branch.

2.2. Characteristics of the DMR

When the PIN diodes loaded at the open end of the DMR resonator are reverse-biased, the DMR is in operation. The schematic of DMR is shown in Fig. 4(a). When the DMR resonator is excited by odd mode, the equivalent circuit is shown in Fig. 4(b). The equivalent admittance Y_{ino2} can be calculated as follows

$$Y_{ino2} = -jY_8 \cot\theta_8 + Y_{load} \tag{8}$$

When the DMR resonator is excited by even mode, the symmetry plane can be equivalent to an open circuit. The equivalent admittance Y_{ine2} in Fig. 4(c) can be calculated as follows

$$Y_{ine2} = jY_8 \left(\frac{2Y_8 \tan\theta_7 \tan\theta_8 - Y_7}{2Y_8 \tan\theta_7 + Y_7 \tan\theta_8} \right) + Y_{load} \tag{9}$$

When DMR resonates, $\text{Im}(Y_{ino2}) = 0$ and $\text{Im}(Y_{ine2}) = 0$. Let $f_{0o1'}$ be the resonant frequency under odd mode excitation and $f_{0e1'}$ be the resonant frequencies under even mode excitation. The two resonant frequencies have the relationship of $f_{0e1'} < f_{0o1'}$. $f_{0o1'}$ is determined by θ_8, and $f_{0e1'}$ is determined by θ_7 and θ_8. The effect of the DMR's branch length on the self-resonant frequency shown in Fig. 5 is consistent with the conclusion of even and odd-mode analysis. During the design process, adjust l_8 to determine the self-resonant frequency $f_{0o1'}$, and then adjust l_7 to tune $f_{0e1'}$.

According to the previous analysis of TMR's PIN diodes' forward bias, when the DMR's PIN diodes are forward biased, the corresponding passband is closed.

2.3. Coupling Routing Scheme

Figure 6 shows the corresponding coupling topology of the proposed switchable dual-band BPF. TMR forms the lower passband, while DMR forms the upper passband. S and L represent the source and load, respectively. E1, O1, and E2 represent the three resonant modes of TMR, while E1′ and O1′ represent the
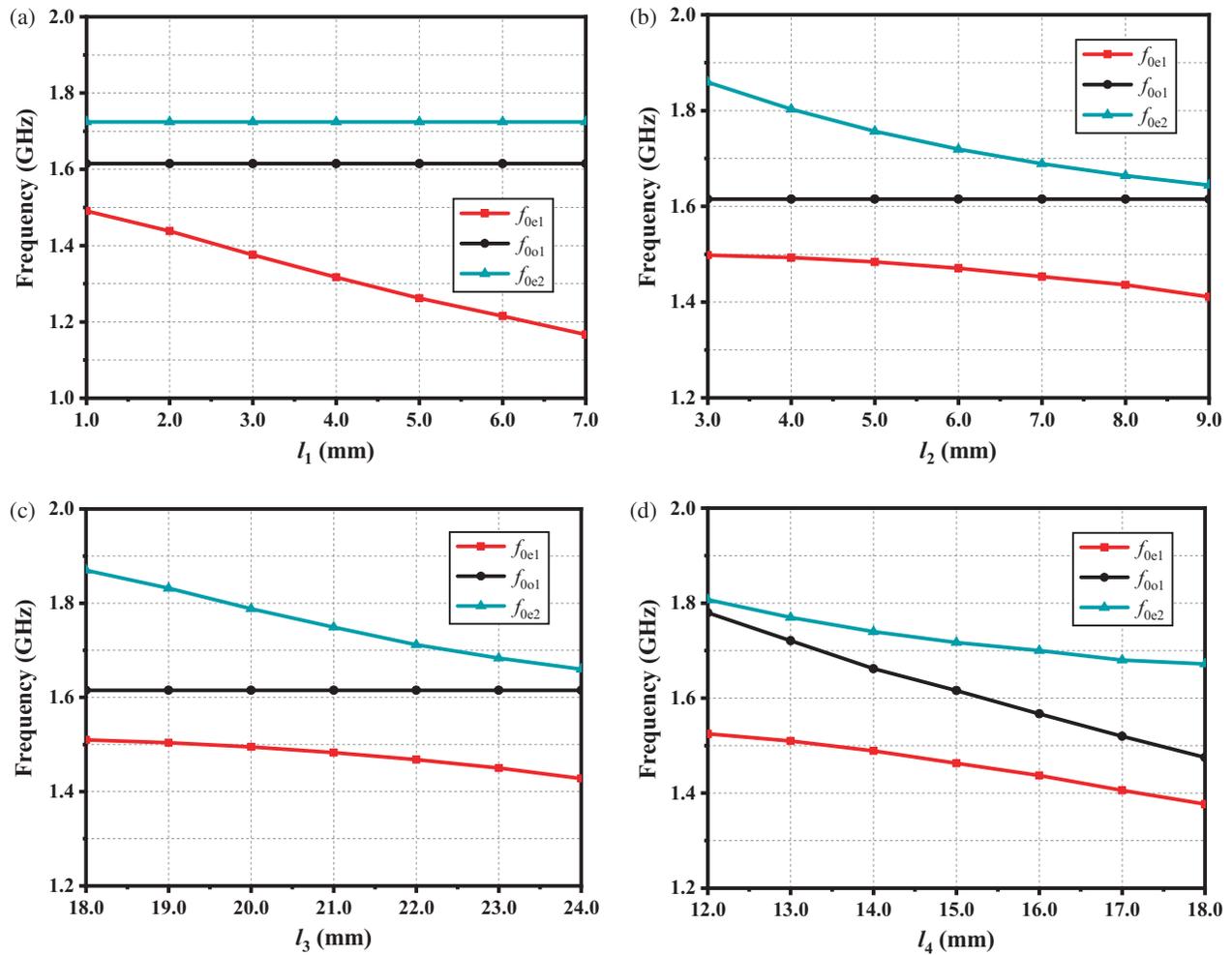
FIGURE 3. Variation of the self-resonant frequency with the changes of (a) l_1, (b) l_2, (c) l_3, (d) l_4.
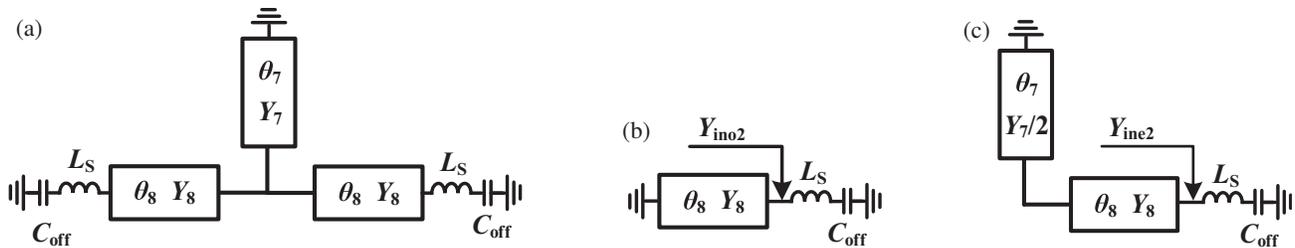

FIGURE 4. (a) Schematic of the DMR. (b) Odd-mode equivalent circuit. (c) Even-mode equivalent circuit.

two resonant modes of DMR. Among them, E represents the even mode, and O represents the odd mode. It is worth noting that each passband has its own transmission path, and the position and bandwidth can be independently controlled. The proposed switchable dual-band BPF can achieve switching of four states, and the truth table is shown in Table 1.

2.4. BPF Design

When diodes D1–D4 are reverse-biased, the lower passband is conducting. The design specification for the conduction state of the lower passband is as follows: it is centered at f_0 of 1.575 GHz with a bandwidth (BW) of 300 MHz and an RL of

18 dB. Design a third-order filter using TMR, and the synthesized passband coupling matrix is shown in (10).

$$[m] = \begin{bmatrix} 0 & 0.469 & -0.6 & 0.345 & 0 \\ 0.469 & 0.866 & 0 & 0 & 0.469 \\ -0.6 & 0 & -0.251 & 0 & 0.6 \\ 0.345 & 0 & 0 & -0.945 & 0.345 \\ 0 & 0.469 & 0.6 & 0.345 & 0 \end{bmatrix} \quad (10)$$

The matrix elements are respectively related to the external quality factor Q_{ei} or the self-resonant frequency f_{0i} of different resonant modes. The self-resonant frequency is determined by
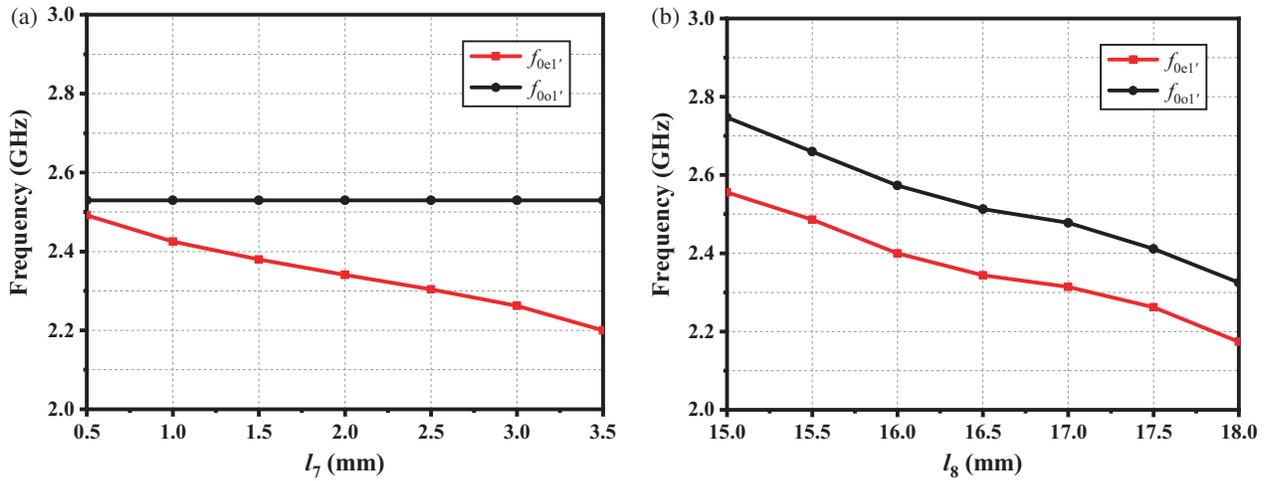
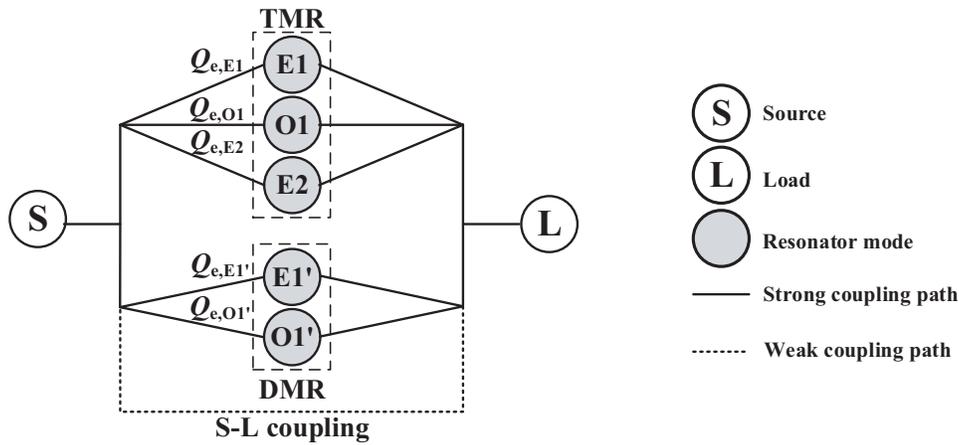**FIGURE 5**. Variation of the self-resonant frequency with the changes of (a) l_7, (b) l_8.

FIGURE 6. Coupling topology of the proposed switchable dual-band BPF.

TABLE 1. Truth table of operation states of the proposed switchable dual-band BPF.

| Operating states	Switch state	Resonator state	Voltages (V)
State 1 (1575 GHz/2450 GHz dual-band BPF)	Switch 1–4: Off	TMR: On	$V_{bias1} = V_{bias2} = 20$
	Switch 5–6: Off	DMR: On	
State 2 (1575 GHz BPF)	Switch 1–4: Off	TMR: On	$V_{bias1} = 20, V_{bias2} = -20$
	Switch 5–6: On	DMR: Off	
State 3 (2450 GHz BPF)	Switch 1–4: On	TMR: Off	$V_{bias1} = -20, V_{bias2} = 20$
	Switch 5–6: Off	DMR: On	
State 4 (ASF)	Switch 1–4: On	TMR: Off	$V_{bias1} = -20, V_{bias2} = -20$
	Switch 5–6: On	DMR: Off	

the following equation [20]:

$$f_{0i} = f_0 \left(1 - \frac{m_{ii} \cdot \text{FBW}}{2} \right) \quad (11)$$

where f_0 is the center frequency (CF) of the BPF passband, and FBW is the fractional bandwidth.

The external quality factor Q_{ei} is calculated by using (12) [20]

$$Q_{ei} = \frac{1}{m_{si}^2 \cdot \text{FBW}} \quad (12)$$

It can be calculated by (10) and (11) that the design parameters for the lower passband are $f_{0E1} = 1.450$ GHz, $f_{0O1} = 1.613$ GHz, $f_{0E2} = 1.723$ GHz, $Q_{e,E1} = 23.87$, $Q_{e,O1} = 14.58$, and $Q_{e,E2} = 44.11$.
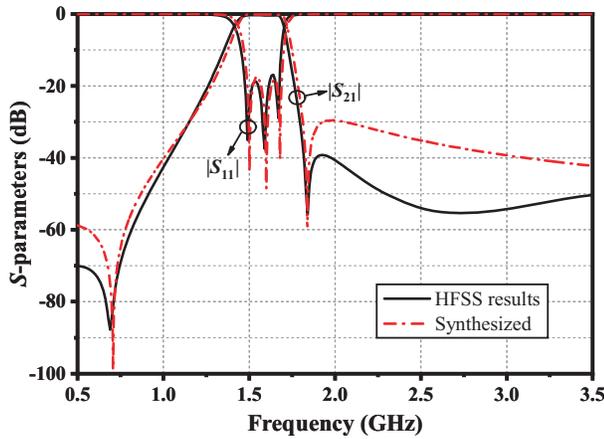
FIGURE 7. Synthesized and HFSS simulated results of the lower pass-band.

FIGURE 8. Synthesized and HFSS simulated results of the upper pass-band.

According to the analysis of TMR in Section 2.1, adjust l_4 and l_5 to determine the self-resonant frequency f_{0O1}, and then tune the self-resonant frequencies f_{0E1} and f_{0E2} by adjusting l_1, l_2, and l_3. The external quality factor Q_{ei} can be extracted as follows [20].

$$Q_{ei} = \frac{\omega_0}{\Delta\omega_{\pm 3\,\text{dB}}} \quad (13)$$

where ω and $\Delta\omega_{\pm 3\,\text{dB}}$ are the CF and 3-dB bandwidth. Q_e is met by adjusting the length l_6 and the distance g_1 between the feed line and TMR resonator, and its value is determined by the equation $Q_e = (Q_{e,E1} + Q_{e,O1} + Q_{e,E2})/3$ [13]. By adjusting these dimensions, a good filtering performance can be obtained for the lower passband.

Figure 7 plots the synthesized and HFSS simulated results of the lower passband, showing good consistency between these two curves. The two transmission zeros (TZs) are obtained by using the TMR resonator.

The upper passband is conducting when diodes D5 and D6 are reverse-biased. A two-pole BPF using DMR with a BW of 210 MHz is designed for the 2.45-GHz filter. The RL is set to 20 dB with two TZs set at 2.08 and 3.01 GHz, respectively. Obtain the following coupling matrix:
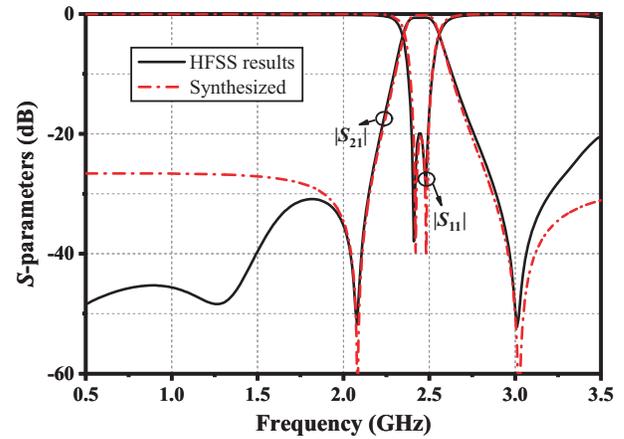
$$[m] = \begin{bmatrix} 0 & -0.541 & 0.564 & 0.023 \\ -0.541 & 0.68 & 0 & 0.541 \\ 0.564 & 0 & -0.702 & 0.564 \\ 0.023 & 0.541 & 0.564 & 0 \end{bmatrix} \quad (14)$$

Calculate according to (11): $f_{0E1'} = 2.380\,\text{GHz}$, $f_{0O1'} = 2.525\,\text{GHz}$. And calculated according to (12): $Q_{e,E1'} = 39.86$, $Q_{e,O1'} = 36.68$. $k_{SL} = m_{SL} \times \text{FBW} = 0.00197$.

Source-loading coupling coefficient k_{SL} can be extracted using (15) [20].

$$k_{SL} = \pm\text{FBW}\frac{1 - \sqrt{1 - |S_{SL}|^2}}{|S_{SL}|} \quad (15)$$

where S_{SL} is the transmission coefficient from the source to the load that only involves the source-loading coupling.

According to the analysis of DMR in Section 2.2, the length of l_8 determines the self-resonant frequency of $f_{0E1'}$, while the lengths of l_7 and l_8 together determine the self-resonant frequency of $f_{0O1'}$. The quality factor $Q_{e'} = (Q_{e,E1'} + Q_{e,O1'})/2$ is determined by the length of the upper passband feed line l_9 and gap g_2, while l_6 also affects the quality factor. By adjusting these dimensions, a good filtering performance can be obtained for the upper passband. Fig. 8 shows the synthesized results of the upper passband, and a good consistency with the HFSS simulated results can be observed. Two TZs are generated by the S-L coupling. Due to a stopband generated by the feed line l_6 of lower passband BPF at 1.3 GHz, there is a deeper suppression.

Figure 9 depicts the effect of the S-L coupling gap g_4 on the upper passband and OSS. It is noted that as the coupling gap increases, the number of TZs decreases from two to one, and the selectivity of the filter deteriorates. However, the OSS performance shows the opposite trend. Therefore, to achieve good OSS performance, the S-L coupling gap g_4 is increased, and the coupling coefficient k_{SL} is optimized to 0.00017.

Next, an open stub with a length of l_{10} is connected in parallel at the feed line to generate a TZ on the upper side of passband. The introduction of an open stub changes the coupling state of the two passbands. After considering this, the coupling matrices of the two passbands are synthesized as follows:

$$[m] = \begin{bmatrix} 0 & 0.458 & -0.6 & 0.315 & 0 \\ 0.458 & 0.916 & 0 & 0 & 0.458 \\ -0.6 & 0 & -0.261 & 0 & 0.6 \\ 0.315 & 0 & 0 & -0.945 & 0.315 \\ 0 & 0.458 & 0.6 & 0.315 & 0 \end{bmatrix} \quad (16)$$

Matrix (16) is the coupling matrix of 1.575-GHz BPF. $f_{0E1} = 1.444\,\text{GHz}$, $f_{0O1} = 1.615\,\text{GHz}$, and $f_{0E2} = 1.723\,\text{GHz}$ can be calculated using (11). $Q_{e,E1} = 25.028$, $Q_{e,O1} = 14.583$, and $Q_{e,E2} = 52.910$ can be calculated using (12).

$$[m] = \begin{bmatrix} 0 & -0.542 & 0.564 & 0.00014 \\ -0.542 & 0.68 & 0 & 0.542 \\ 0.564 & 0 & -0.702 & 0.564 \\ 0.00014 & 0.542 & 0.564 & 0 \end{bmatrix} \quad (17)$$
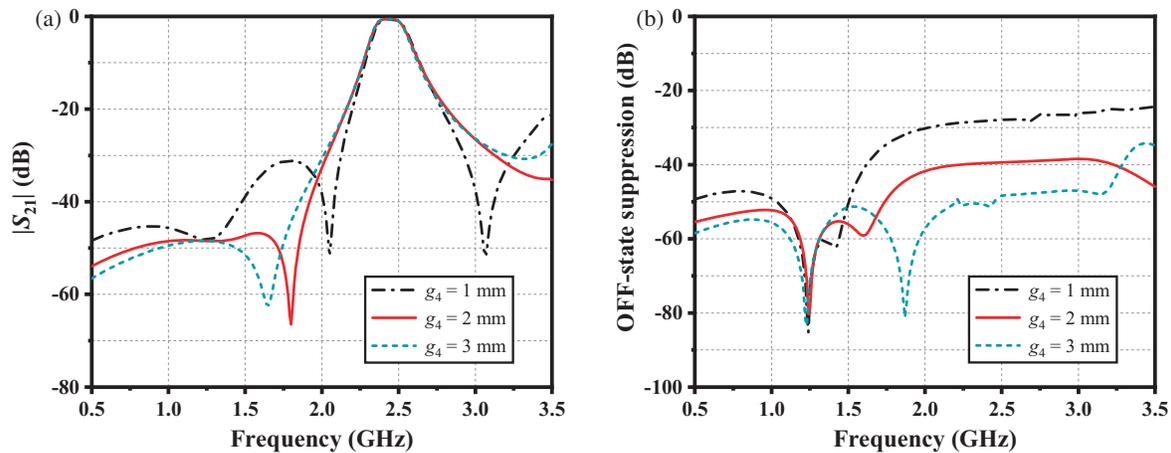
FIGURE 9. Effect of g_4 on the (a) upper passband, (b) OSS.

Matrix (17) is the coupling matrix of 2.45 GHz BPF. $f_{0E1'} = 2.380$ GHz and $f_{0O1'} = 2.525$ GHz can be calculated using (11). $Q_{e,E1'} = 39.71$ and $Q_{e,O1'} = 36.68$ can be calculated using (12). $k_{SL} = m_{SL} \times$ FBW $= 0.000012$.

Figure 10 compares the dual-band BPFs with or without open stub. It can be seen that the open stub introduces two TZs at 2.98 GHz and 3.13 GHz, which improves the selectivity of the passband and enhances the suppression performance of the stopband.
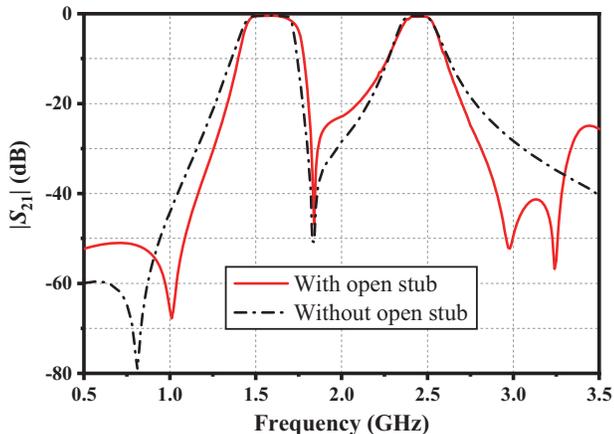

FIGURE 10. Simulated performances of the State 1 (dual-band BPF) with or without open stub.

2.5. Design Procedure

Based on the above analysis and discussions, a design procedure of the proposed four-state switchable dual-band bandpass filter can be summarized as follows.

1) Determine the required CF, BW, RL, and the position of TZs. Based on the design specification of dual-band BPF, the coupling matrix is synthesized [20]. Use TMR and DMR to achieve two passbands respectively, and reduce the size of the resonator through step impedance and folding. The initial electrical parameters are obtained by modeling in ADS to determine the initial size.

2) Optimize the two passbands' OSS performance respectively. The diodes are loaded on the open ends of the resonator to obtain a better OSS performance. It can be seen from Fig. 9 that introducing source-load coupling would greatly lessen the OSS performance. Therefore, in subsequent designs, the source-load coupling should be reduced or avoided.

3) Place the two passband structures together for electromagnetic simulation. If the resonator is excessively folded, it will introduce some unexpected spurious passbands. The shape of the resonator should be adjusted to avoid the occurrence of unexpected spurious passbands. The impedance of the feed lines should be selected appropriately; otherwise, it will cause an increase in IL in one of the passbands. Reducing interference between two passbands includes three aspects: (i) Two passbands are arranged vertically and separated by a certain distance. (ii) Adjust the position of the input and output ports. (iii) Adjust the position of the transmission zeros of two passband structures.

4) Optimize the performance of switchable filters. An open stub is introduced at an appropriate position to improve the passband selectivity and stopband suppression performance (as shown in Fig. 10), and then finely tune the size of the filter to achieve optimal performance.
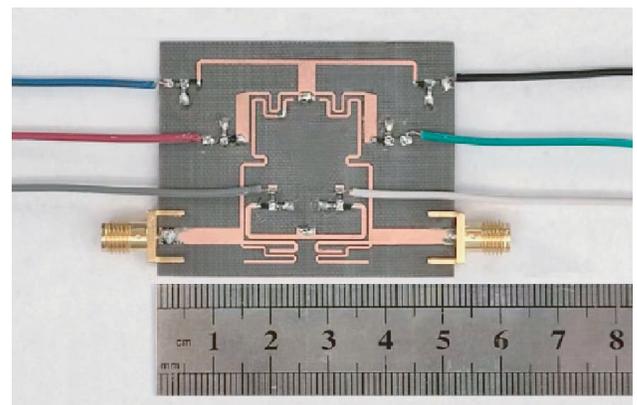

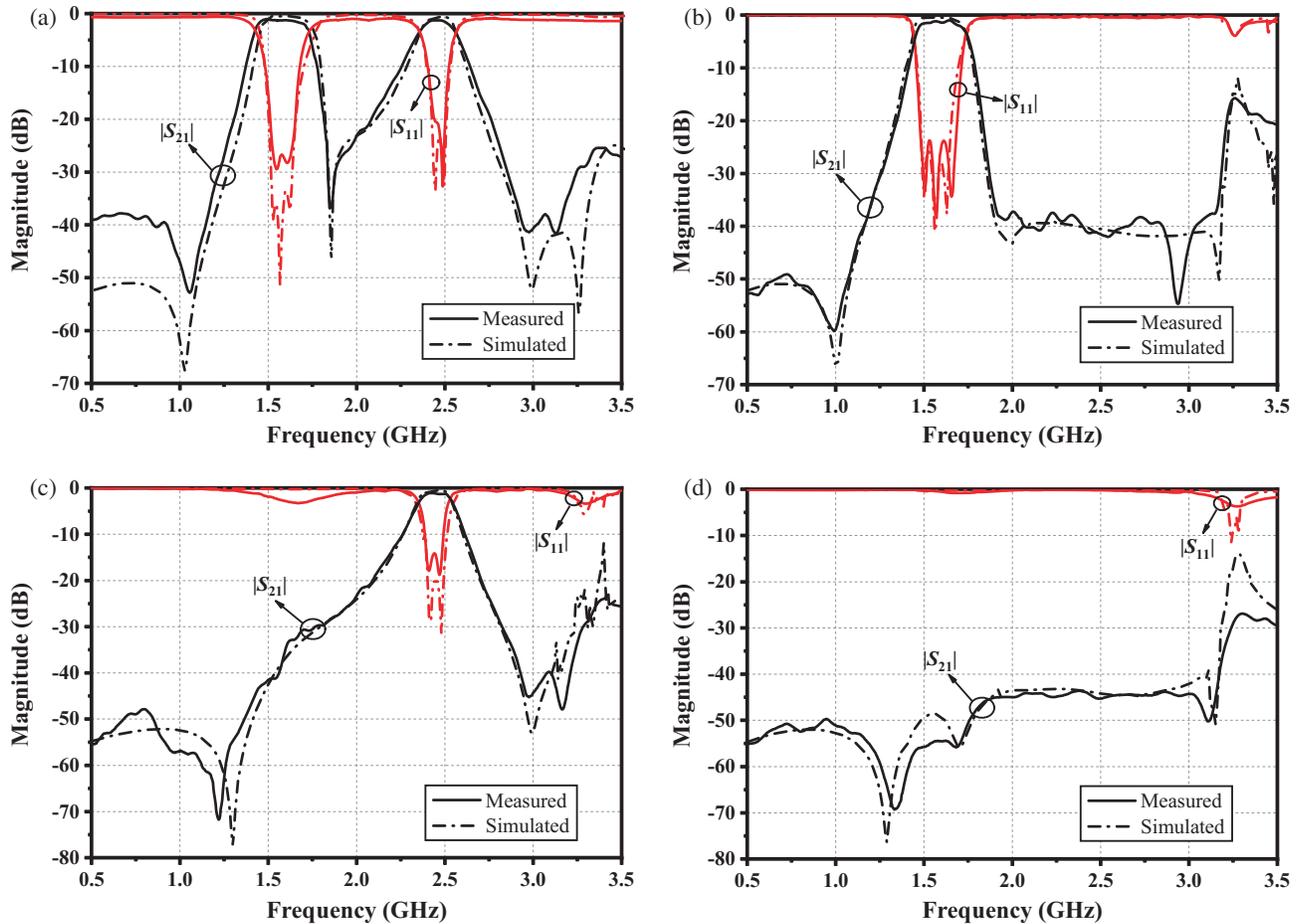**FIGURE 11**. Photograph of the fabricated switchable dual-band BPF.

FIGURE 12. Simulated and measured results of the proposed switchable dual-band BPF. (a) State 1. (b) State 2. (c) State 3. (d) State 4.

3. SIMULATED AND MEASURED RESULTS

Figure 11 shows a photograph of the manufactured switchable dual-band BPF with a circuit area of $0.128\lambda_g^2$, where λ_g is the guided wavelength at 1.575 GHz. The switchable dual-band BPF proposed in this paper uses an F4B substrate with a thickness of 1 mm, relative permittivity of 2.65, and loss tangent of 0.003. SMP1345-079LF PIN diodes are used. The physical dimensions of the switchable dual-band BPF are as follows: $l_1 = 1.25$, $l_2 = 5.83$, $l_3 = 21.6$, $l_4 = 14.6$, $l_5 = 8.28$, $l_6 = 41.84$, $l_7 = 1.1$, $l_8 = 16.15$, $l_9 = 15.12$, $l_{10} = 21.3$, $w_1 = 2.75$, $w_2 = 3$, $w_3 = 0.66$, $w_4 = 0.44$, $w_5 = 2.2$, $w_6 = 0.6$, $w_7 = 3.31$, $w_8 = 0.8$, $w_9 = 0.6$, $w_{10} = 0.4$, $g_1 = 0.48$, $g_2 = 0.3$, $g_3 = 0.3$, $g_4 = 3$, $g_5 = 3.44$ (unit: mm). Fig. 12 shows the simulation and measurement results of the proposed switchable dual-band BPF.

When $V_{bias1} = V_{bias2} = 20$ V, diodes D1–D6 are reverse-biased, and the filter is in a dual-band bandpass response state. Fig. 12(a) shows the simulated and measured results of the dual-band response state for a switchable dual-band BPF. The measured CF and 3-dB FBW of the lower passband are 1.58 GHz and 19.97%. The upper passband has a CF of 2.46 GHz and 3-dB FBW of 9.45%. The RL and IL of the two passbands were measured to be better than 26.7 dB/20.5 dB and

1.05 dB/1.27 dB, respectively. Four TZs can be observed at 1.055 GHz, 1.850 GHz, 2.98 GHz, and 3.13 GHz.

When $V_{bias1} = 20$ V and $V_{bias2} = -20$ V, diodes D1–D4 are reverse-biased, and D5 and D6 conduct forward. At this time, the lower passband is in a responsive state. The simulated and measured results at lower passband responsive state are shown in Fig. 12(b). The lower passband has a CF of 1.60 GHz and 3-dB FBW of 18.36% The measured RL and IL are better than 23.8 dB and 1.02 dB, respectively. Currently, the OSS at the upper band is as high as 41.2 dB. Two TZs can be observed at 1.01 GHz and 2.94 GHz.

When diodes D1–D4 conduct, D5 and D6 are reverse-biased; TMR is detuned; the upper passband is in a responsive state. As shown in Fig. 12(c), the CF is measured at 2.45 GHz with a 3 dB FBW of 8.75%. It can be observed that the measured RL and IL are better than 14.1 dB and 1.09 dB, respectively. Currently, the OSS at the lower band is as high as 38.3 dB. Three TZs can be observed at 1.22 GHz, 2.98 GHz, and 3.16 GHz.

When all switches are turned on, both DMR and TMR are detuned, and the filter is in an ASF state. As shown in Fig. 12(d), the measured OSS at 1.575 GHz and 2.45 GHz are better than 51.03 dB and 43.61 dB, respectively.

Table 2 gives a performance comparison with some related references. It can be seen that the OSS of [12] and [15] is

TABLE 2. Comparison with related references.

References	f_0 (GHz)	State	IL (dB)	RL (dB)	FBW (%)	OSS at f_0 (dB)	OSS of all-stop filter (dB)	Filter size (λ_g^2)
[12]	2.90/4.79	4	1.2/1.1	$> 10/ > 20$	6.2/5.9	19.3/17.8	> 18.1	0.16
[13]	3.15/4.20	3	~ 4	$> 9/ > 12$	-	~ 25	-	0.679
[14]	0.89/1.82	4	2.06/2.05	$> 18.7/ > 18.4$	8.3/9.6	44.4/39.9	-	0.061
[15]	0.9/2.35	4	1.4/4.9	-	8.9/8.4	23.7/28.0	> 25.0	0.07
This work	1.58/2.46	4	1.05/1.27	$> 26.7/ > 20.5$	19.97/9.45	41.2/38.3	> 43.6	0.128

lower than 25 dB in the all-stop state, while [13] and [14] cannot achieve all-stop state. The proposed dual-band switchable BPF achieves an OSS of 43.6 dB in the all-stop state. Secondly, the IL of both passbands for this work is relatively lower. The IL in [13–15] is greater than 2 dB, while the IL in this paper is within 1.3 dB. Besides, the RL performance of this work is excellent. Compared with the previous filters [12–15], this work achieves an RL of over 20 dB within each operating passband, which indicates good matching characteristics.

In summary, compared with the previous filters [12–15], the proposed four-state switchable dual-band bandpass filter not only has low insertion loss and good matching characteristics with compact circuit size, but also can achieve a great OFF-state suppression of 43.6 dB in the all-stop state, allowing the transmission of the desired signals while eliminating unwanted agile interferers.

4. CONCLUSION

This paper has presented a method for designing a switchable dual-band BPF using multi-mode resonators and PIN diodes. Each passband has an independent coupling path, so it can be controlled independently. There are four operating modes: 1.575-GHz BPF mode, 2.45-GHz BPF mode, dual-band BPF mode, and ASF mode. Detailed design methods are provided. The measured results show that the proposed switchable dual-band BPF exhibits low IL, high OSS, and compact size.

ACKNOWLEDGEMENT

REFERENCES

[1] Xu, K.-D., S. Xia, Y. Jiang, Y.-J. Guo, Y. Liu, R. Wu, J. Cui, and Q. Chen, "Compact millimeter-wave on-chip dual-band bandpass filter in 0.15-µm GaAs technology," *IEEE Journal of the Electron Devices Society*, Vol. 10, 152–156, Jan. 2022.

[2] Xu, Z., Y. Wu, S. Li, Z. Wang, and W. Wang, "Exhaustive design and realization for in-line topology quasi-TEM mode dielectric waveguide filter with dispersive couplings," *IEEE Transactions on Circuits and Systems II: Express Briefs*, Feb. 2024.

[3] Liu, H., J. Kuang, Y. Cao, and Y. Zhang, "Flexible design of dual-band common-mode filters using hairpin ring resonators and defected ground slots," *IEEE Transactions on Electromagnetic Compatibility*, Vol. 65, No. 5, 1360–1370, Oct. 2023.

[4] Lee, J.-E., J.-H. Song, M.-S. Baek, J.-T. Son, J.-H. Kim, E.-G. Lee, S. Choi, and C.-Y. Kim, "A sub-6 GHz asymmetric GaAs SPDT switch with high Tx-to-Rx isolation and low insertion loss," *IEEE Microwave and Wireless Technology Letters*, Vol. 34, No. 5, 490–492, May 2024.

[5] Sun, Z., X. Wang, and K. Li, "A switchable bandpass filter for broadband, dual-band and tri-band operations," *IEEE Transactions on Circuits and Systems II: Express Briefs*, Vol. 70, No. 1, 111–115, Jan. 2023.

[6] Xu, J., "A microstrip switchable filter with four operating modes," *IEEE Microwave and Wireless Components Letters*, Vol. 26, No. 2, 101–103, Feb. 2016.

[7] Li, D. and K.-D. Xu, "Multifunctional switchable filter using coupled-line structure," *IEEE Microwave and Wireless Components Letters*, Vol. 31, No. 5, 457–460, May 2021.

[8] Song, K., W. Chen, S. R. Patience, Y. Chen, A. M. Iman, and Y. Fan, "Compact wide-frequency tunable filter with switchable bandpass and bandstop frequency response," *IEEE Access*, Vol. 7, 47503–47508, 2019.

[9] Bandyopadhyay, A., P. Sarkar, T. Mondal, and R. Ghatak, "A dual function reconfigurable bandpass filter for wideband and tri-band operations," *IEEE Transactions on Circuits and Systems II: Express Briefs*, Vol. 68, No. 6, 1892–1896, Jun. 2021.

[10] Feng, W., Y. Shang, W. Che, R. Gómez-García, and Q. Xue, "Multifunctional reconfigurable filter using transversal signal-interaction concepts," *IEEE Microwave and Wireless Components Letters*, Vol. 27, No. 11, 980–982, Nov. 2017.

[11] Xie, S., X. Guan, P. Gui, B. Ren, C. Wang, and J. Zhao, "Switchable dual-band bandpass filter with four-state frequency responses," in *2019 International Conference on Microwave and Millimeter Wave Technology (ICMMT)*, 1–3, Guangzhou, China, 2019.

[12] Ge, J. and G. Wang, "Switchable dual-band bandpass filter with high selectivity," in *2021 IEEE MTT-S International Wireless Symposium (IWS)*, 1–3, Nanjing, China, 2021.

[13] Yan, Z., X. Zhang, X. He, Y. Ye, B. Hou, C. Hu, and W. Wen, "A high performance dual-band switchable bandpass filter and its application in 5G signal detector," *IEEE Transactions on Components, Packaging and Manufacturing Technology*, Vol. 13, No. 8, 1242–1253, Aug. 2023.

[14] Xu, J., F. Liu, and Z.-Y. Feng, "Single-/dual-band bandpass filter-integrated single-pole double-throw switch using distributed coupling tri-mode resonators," *IEEE Transactions on Microwave Theory and Techniques*, Vol. 68, No. 2, 741–749, Feb. 2020.

[15] Chuang, M.-L. and M.-T. Wu, "Switchable dual-band filter with common quarter-wavelength resonators," *IEEE Transactions on Circuits and Systems II: Express Briefs*, Vol. 62, No. 4, 347–351, Apr. 2015.

[16] Tang, C.-W. and J.-M. Jiang, "Design of the microstrip bandpass filter with 4 band-switching modes," *IEEE Transactions on Circuits and Systems II: Express Briefs*, Vol. 70, No. 6, 1926–1930, Jun. 2023.

[17] Tseng, H.-Y., C.-F. Chen, Y.-H. He, K.-W. Zhou, and R.-Y. Chen, "A microstrip two-state switchable dual-band bandpass filter," in *2020 IEEE Asia-Pacific Microwave Conference (APMC)*, 761–763, Hong Kong, 2020.

[18] He, Y.-H., C.-F. Chen, H.-Y. Tseng, and W.-J. Li, "A switchable dual-band bandpass filter with flexible band allocation," in *2021 IEEE International Symposium on Radio-Frequency Integration Technology (RFIT)*, 1–3, Hualien, Taiwan, 2021.

[19] Xu, J., Q.-H. Cai, Y.-F. Guo, S.-Y. Ji, and Y.-W. Duan, "A BPF integrated SP4T switch using parallel switched fractal common feeding line," *IEEE Transactions on Circuits and Systems II: Express Briefs*, Vol. 68, No. 6, 1932–1936, Jun. 2021.

[20] Hong, J.-S. and M. J. Lancaster, *Microstrip Filters for RF/Microwave Applications*, John Wiley & Sons, 2001.